

A Rule of Solute Segregation at Grain Boundaries

Xin Li, Wang Gao*, and Qing Jiang

Key Laboratory of Automobile Materials, Ministry of Education, Department of Materials Science and Engineering, Jilin University, 130022, Changchun, China

The control of solute segregation at grain boundaries (GBs) is essential in engineering alloy properties, however the structure-activity relationship of the key parameter—the segregation energies—still remains elusive. Here we propose the electronic and geometric descriptors of GB segregation based on the valence, electronegativity and size of solutes and the non-local coordination number of free surfaces, with which we build a predictive framework to determine the segregation energies across different solutes, matrices, GB structures and segregation sites. This framework uncovers not only the coupling rule of solutes and matrices in GB segregation, but also the origin of solute-segregation determinants. The contribution of solutes essentially stems from their d- and s-state coupling in alloying, whereas that of matrix GB interfaces is determined by matrix free surfaces. Our scheme builds a novel picture for the solute segregation at GBs and provides a useful tool for the design of advanced alloys.

Solute segregation at grain boundaries (GBs) plays an essential role in governing the mechanical, functional, and kinetic properties of metallic materials because it controls the chemical composition and local structure of GBs¹⁻⁴. This critical segregation behavior can be quantitatively characterized by the segregation energies, which measure the preference of solute atoms to segregate to GBs or remain inside the bulk. Generally, the segregation energies depend on the electronic and geometric properties of solutes and matrices. However, it still presents a fundamental challenge to rapidly evaluate the GB segregation energies and to understand the underlying mechanism of solute segregation.

While many studies of segregation energies focus on the numerical calculations of individual systems using density functional theory (DFT) and molecular dynamics methods⁵⁻¹², some frameworks have been proposed for predicting the segregation energies. Early empirical thermodynamic models correlated the segregation energies with macroscopic properties, such as the bulk modulus and shear modulus in the McLean model¹³ and the bonding energy differences between solutes and matrix atoms in the Miedema model^{14,15}. However, these models rarely explain the electronic origin of GB segregation and are rather limited in predicting the segregation energies^{16,17}. Some machine learning methods can be used to predict the segregation energies accurately^{18,19}, but generally cannot provide a clear physical picture of segregation behaviors. Other effective descriptors were also proposed to describe the segregation energies, such as the parameters based on the d-band properties²⁰⁻²², excess volume²³ and coordination number¹⁸. Essentially these descriptors characterize the structures of matrices, however, none of them can reflect the electronic effect of solutes. In addition, some descriptors like the d-band properties and excess volume, derived from density functional theory (DFT) calculations, are time-consuming to obtain and even with some numerical uncertainties. Moreover, they are hardly applicable to complicated GBs such as those in polycrystals.

Here, we find that the valence, electronegativity and size of solutes combined together with the generalized coordination number of segregation sites control the

segregation energies. With these easily accessible parameters, we build a predictive framework for evaluating the segregation energies across the different solutes, matrices, GBs and segregation sites. This framework reveals that the solute effect of GB segregation originates from the solute d- and s-state coupling in alloying and the matrix interface effect from the matrix free surfaces. These results provide a deep understanding of the GB-segregation mechanism and a physical guidance for designing the alloy structures with targeted properties.

Results

The effect of different solutes in matrices. First, we focus on the role of different transition metal (TM) solutes in GB segregation. Generally, the shift of a solute atom from the matrix to GBs involves the bond breaking and forming and is limited by the volume of segregation sites. We thus attempt to describe the segregation behaviors from the cohesive force and interatomic bond strength of solutes and from the size of solutes. Tight-binding (TB) and Friedel's models^{24,25} have revealed in TMs that the d-band width is dominant in the formation of the cohesive force and the s-band contribution dictates the mole volume and compressibility²⁶. It is known that the d-band width depends strongly on the valence-electron number (S_v) and the interatomic bond strength is correlated with Pauling electronegativity (χ). We thus adopt $\psi = \frac{S_v^2}{\chi}$, which can describe the surface bond breaking reasonably^{27,28}, to study the segregation energies (E_{seg}). ψ is found to provide a rough description of the trend of the segregation energies in the W matrix from Supplementary Fig. 1. Furthermore, we introduce the size effect of solutes on the top of ψ by only taking into account the two-body effect with a Lennard-Jones (L-J) potential like formula as follows,

$$D_{\text{seg}} = \left[\left(\frac{\sigma}{R} \right)^{12} - \left(\frac{\sigma}{R} \right)^6 \right] \times \psi = \left[\left(\frac{\sigma}{R} \right)^{12} - \left(\frac{\sigma}{R} \right)^6 \right] \times \frac{S_v^2}{\chi} \quad (1)$$

Here, R is the atom radius of solute atoms. σ is a constant 1.21. All the parameters in D_{seg} can be obtained by table looking up (Supplementary Table 1).

We first study the solute segregation at the ideal W GBs,

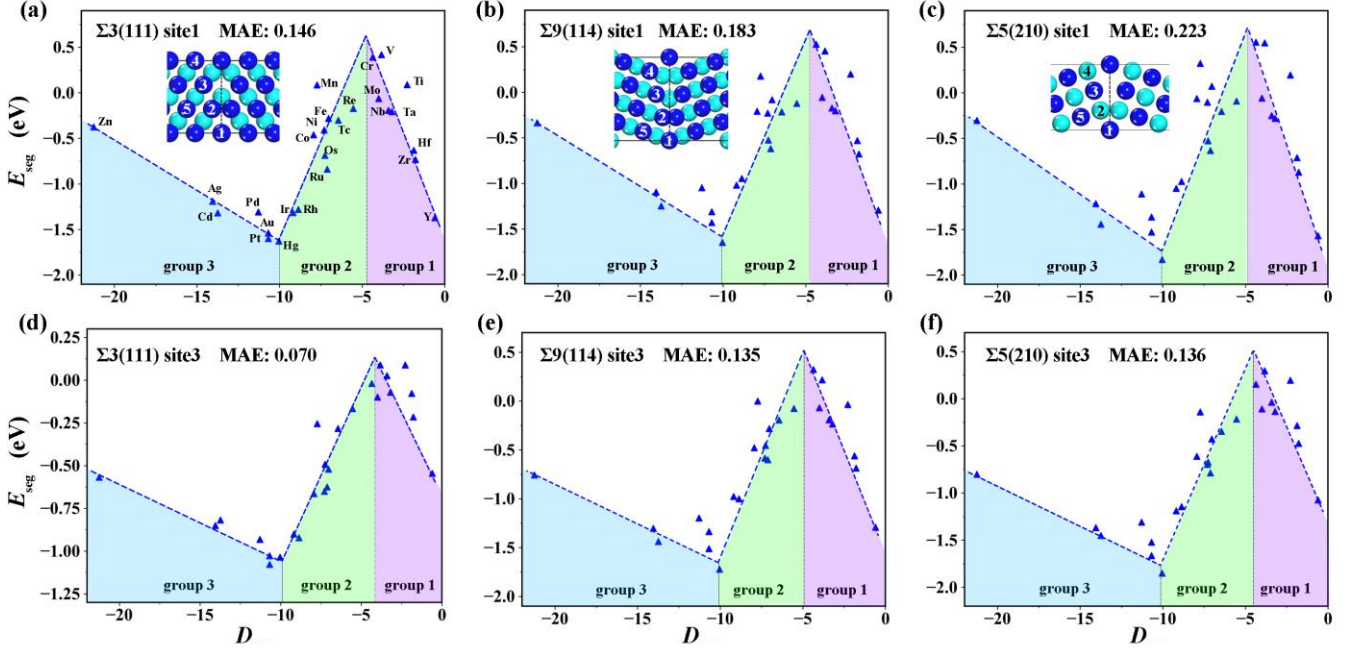


Fig. 1 The segregation energies of solutes as a function of the descriptors D_{seg} at different W GBs and segregation sites. (a) The segregation site1 of $\Sigma 3(111)$ GB, (b) The segregation site1 of $\Sigma 9(114)$ GB, (c) The segregation site 1 of $\Sigma 5(210)$ GB, (d) The segregation site3 of $\Sigma 3(111)$ GB, (e) The segregation site3 of $\Sigma 9(114)$ GB, and (f) The segregation site3 of $\Sigma 5(210)$ GB. The structures of the three GBs and corresponding substitution sites are illustrated in the subgraphs of (a)-(c).

by adopting 8 symmetric tilt GB structures ($\Sigma 3(111)$, $\Sigma 3(112)$, $\Sigma 5(210)$, $\Sigma 5(310)$, $\Sigma 7(213)$, $\Sigma 9(114)$, $\Sigma 11(323)$ and $\Sigma 13(510)$) with five different substitution sites along each GB structure (The structures and substitution sites are illustrated in Fig. 1 and Supplementary Fig. 2). The results show that E_{seg} scales with D_{seg} in a broken-line relationship for the considered TM solutes with reasonable accuracy regardless of the GB structures and segregation sites (Fig.1 and Supplementary Table 2). The turning point of the broken-line scaling is around $D_{\text{seg}} = -5$ (Cr and V) and $D_{\text{seg}} = -10$ (Hg and Au), dividing the solutes into the three groups (see Fig. 1).

These results essentially originate from the different d- and s-state properties of TM atoms in alloying. The TB model shows that the d-band width dominates the trend of the cohesive force of IIIB-VIII group TMs and the s-bands dictate that of the IB and IIB group TMs. The behavior of the solutes in groups 1 and 2 follows the trend of the cohesive energy of IIIB-VIII group TMs, reflecting the dominant role of the d-states in alloying IIIB-VIII group solutes with W. On the other hand, the behavior of the solutes in group 3 is opposite to that in group 2, corresponding to the dominant role of the s-states in alloying IB-IIB group solutes with W²⁶. For $\psi = \frac{S_v^2}{\chi}$, S_v reflects the d-band filling in IIIB-VIII group TMs because the s-band filling is nearly constant, and does the s-band filling in IB-IIB group TMs because the d-band filling is constant. Meanwhile, ψ correlates with the d-band width and cohesive energy in a rough piecewise linear manner (see Supplementary Fig. 3). It is thus able to capture approximately the segregation behavior of TM solutes (see

Supplementary Fig. 1).

The size effect is secondary compared to the electronic bonding of solutes, in stark contrast with the viewpoints that proposed the solute-size effect to play a major role in GB segregation^{5,6}. A L-J potential like formula²⁹ of D_{seg} implies that the size of solutes exhibits mainly a two-body effect in GB segregation with negligible many-body effects. As ψ reflects the d-band width and s-band filling and the size of solutes does significantly the s-band depth, the descriptor D_{seg} uncovers the coupling nature between the d- and s-states of solutes in determining the segregation energies.

For the three group solutes in W, the corresponding slopes and intercepts of the linear scaling are labeled with k_i and b_i ($i=1-3$). Notably, k_1 , k_2 and k_3 are linearly correlated with each other for all the GBs and segregation sites (see Fig. 2(a) and (b)), and so are b_1 , b_2 and b_3 (see Fig. 2(c) and (d)). Interestingly, for each solute group, the slope is also linearly related to the intercept, such as k_2 and b_2 (Fig. 2(e)). These results indicate a sole physical origin for all slopes and intercepts (that will be further discussed below).

We now consider the segregation energies in W with GB relaxation during solute segregation. For $\Sigma 5(210)$, $\Sigma 7(213)$, $\Sigma 9(114)$, $\Sigma 11(323)$ and $\Sigma 13(510)$ GBs, they experience GB sliding or migration and lose their mirror symmetry^{5,30,31} (see Supplementary Fig. 4). Nevertheless, D_{seg} still exhibits the ability to describe the trends of the segregation energies for various GBs and segregation sites (see Supplementary Fig. 5 and Supplementary Table 3), further indicating that D_{seg} reflects the core elements of the

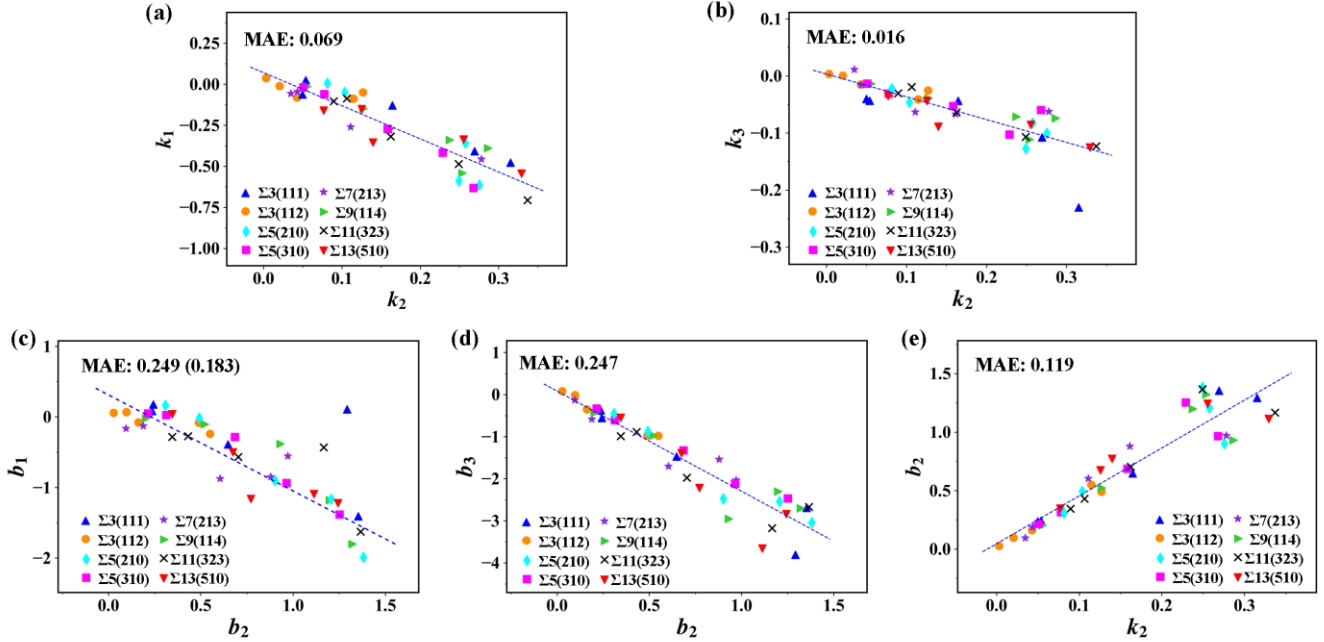


Fig. 2 The linear scaling relationship of slopes and intercepts of different transition-metal solute groups. (a) The relationship of slopes k between group 1 and group 2. (b) The relationship of slopes k between group 3 and group 2. (c) The relationship between the slopes k of group 2 and the intercept b of group 2. The MAE in parentheses is the accuracy without the two outliers. (d) The relationship of intercepts b between group 1 and group 2. (e) The relationship of intercepts b between group 3 and group 2.

electronic bonding and size effects of TM solutes for GB segregation.

In the case of other metal matrices, such as Al, Ni, Zr and Mo, we find that D_{seg} is also able to describe their GB segregation, always exhibiting a broken-linear relationship of E_{seg} vs D_{seg} ^{17,32-35} (Fig. 3 and Supplementary Fig. 6). Based on the segregation energies of solutes in W, Al, Ni, Zr and Mo, we infer that the interactions between solutes and matrices lead to the d^5 state at the turning point of groups 1 and 2 and the d^{10} state at that of groups 2 and 3. Taking the Al matrix as an example, an Al atom has three valence electrons and forms the d^5 state with Ti ($3d^2$) and the d^{10} state with Co ($3d^7$) at the turning points. Importantly, this feature is crucial for the prediction of segregation energies.

Furthermore, D_{seg} is also applicable to the solute segregation of twist GBs and even polycrystal GBs. D_{seg} exhibits a broken-linear relationship with E_{seg} in Mo $\Sigma 5(100)$ twist GB with the mean absolute error (MAE) of 0.169 eV (Fig. 3(d)) on site1 and 0.094 eV on site0 (Supplementary Fig. 6(d)). More importantly, it can describe the trend of segregation energies for the same substitute sites in polycrystals of various matrices such as Ti, Zr, Ta, Co, Ni, Mo, Pd, Pt, Au, Ag and Cu, with the accuracy of 0.05 eV (see Supplementary Fig. 7), comparable to that of the smooth overlap of atomic positions (SOAP) based machine learning work¹⁹. Interestingly, some main-group elemental solutes also follow the D_{seg} -determined relations of TM solutes, indicating that the valence origin of D_{seg} is useful to

understand the behavior of all kind solutes (see Supplementary Fig S6(b)).

Overall, all the above findings demonstrate that the descriptor D_{seg} quantifies effectively the electronic bonding and size effects of solutes at the GB segregation across different kind GBs and matrices.

The geometric effects of matrix GBs. We now attempt to understand the geometric effects of GB structures in segregation behavior, which corresponds to the various GB interfaces and the environment of segregation sites. These effects are influenced by many factors such as GB interface sliding and migration as well as the local deformation. We start with the simple free surfaces (that form GB structures) and use the generalized coordination numbers (\overline{CN}) of free surfaces to characterize GB geometric properties. The expression of \overline{CN} is as follows:

$$\overline{CN}^{(m)} = \frac{\sum_{i=1}^n \overline{CN}^{(m-1)}(i)}{CN_{\text{max}}} \quad (2)$$

Here, i represents the i th neighbor of a given surface atom. n is the number of neighboring atoms. CN_{max} is the max coordination number in the bulk. m denotes the order of approximation. The ordinary coordination number CN corresponds to the zeroth order approximation $\overline{CN}^{(0)}$, describing the geometric environment of a surface atom with its nearest neighbors. We use the first-order approximation $\overline{CN}^{(1)}$, that is, the effect of second-neighboring atoms is

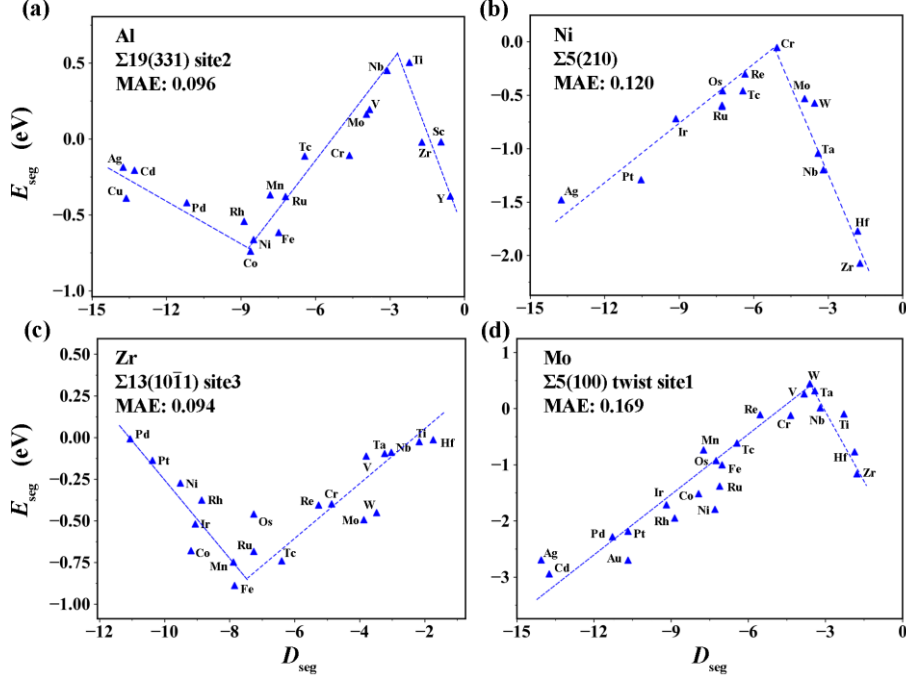


Fig. 3 The correlation between segregation energies and D_{seg} for various matrix GBs. (a) the Al $\Sigma 19(331)$ GB, (b) the Ni $\Sigma 5(210)$ GB, (c) the Zr $\Sigma 13(10\bar{1})$ GB and (d) the Mo $\Sigma 5(100)$ twist GB.

included. Notably, this approximation was first proposed to describe the adsorption of small molecules on TM surfaces and nanoparticles^{36,37}. If one adopts the second- or higher-order approximation of $\overline{CN}^{(m)}$ ($m \geq 2$), the effects of more far neighboring atoms are involved.

Fig. 4(a-c) shows that for the same solute atoms segregated in the ideal W matrix, E_{seg} scales with the $\overline{CN}^{(1)}$ of the segregation sites on the free surfaces in a broken-linear function for each GB. Moreover, most of the segregation sites comply with the same $\overline{CN}^{(1)}$ -determined relation. The error is around 0.2 eV that is within that of the DFT semi-local functional calculations. $\overline{CN}^{(2)}$ is almost the same as $\overline{CN}^{(1)}$ in describing E_{seg} (see Supplementary Fig. 8), indicating that the geometric effect of a segregation site is mainly from its nearest and second-nearest neighbors with a negligible contribution from more far neighbors. The turning point of the broken-linear scaling is around $\overline{CN}^{(1)} = 4$, which is roughly the boundary between site1 and site2. The reverse folding of the site1 likely stems from the fact that the structure of site1 at GBs is close to that of the bulk, thus the corresponding $\overline{CN}^{(1)}$ is larger than that of the free surfaces. Besides the ideal W matrix, the relation determined by the $\overline{CN}^{(1)}$ of the free surfaces also holds for the GBs with the sliding and migration during solute segregation (see Supplementary Fig. 9). These results imply that the geometric contribution of matrix GBs to the segregation energies is non-local compared with the effect of solutes and mainly determined by the ideal matrix free surfaces

regardless of the GB deformation.

Our findings are also comparable to the literature results. Hu *et al.* considered the geometric effect of W and Ta GB matrices with the linear combination of the bimodality property of the d-bands and the strength of sp-d hybridization in the GB structures (that are obtained by DFT calculations)²⁰. $\overline{CN}^{(1)}$ is found to scale with their descriptors, supporting the effectiveness of $\overline{CN}^{(1)}$ in evaluating the GB segregation. Huber *et al.* use the excess volume and ordinary CN to determine the geometric effect of segregation sites and the excess volumes are calculated from the relaxed GB structures with DFT calculations^{18,23}. Compared with the previous descriptors, $\overline{CN}^{(1)}$ originates from the free surfaces and is independent of DFT calculations, avoiding the numerical uncertainty.

A general scheme to determine the segregation energies.

Interestingly, from Fig. 4(d) and Supplementary Fig. 9(d) we find that the slopes k of the scaling between E_{seg} versus D_{seg} are determined by the geometric structures of the matrix GBs, which can be characterized as a function of $\overline{CN}^{(1)}$. We thus propose an entire expression to describe E_{seg} for the group 2 solutes (~ 15 TM elements) in the ideal W GBs:

$$E_{\text{seg}} = \begin{cases} (0.15 \overline{CN}^{(1)} - 0.3) (D_{\text{seg}} + 4), & \overline{CN}^{(1)} \leq 4 \\ (-0.08 \overline{CN}^{(1)} + 0.67) (D_{\text{seg}} + 4), & \overline{CN}^{(1)} > 4 \end{cases} \quad (3)$$

According to the linear correlations of the slopes and intercepts for the three solute groups, one can determine

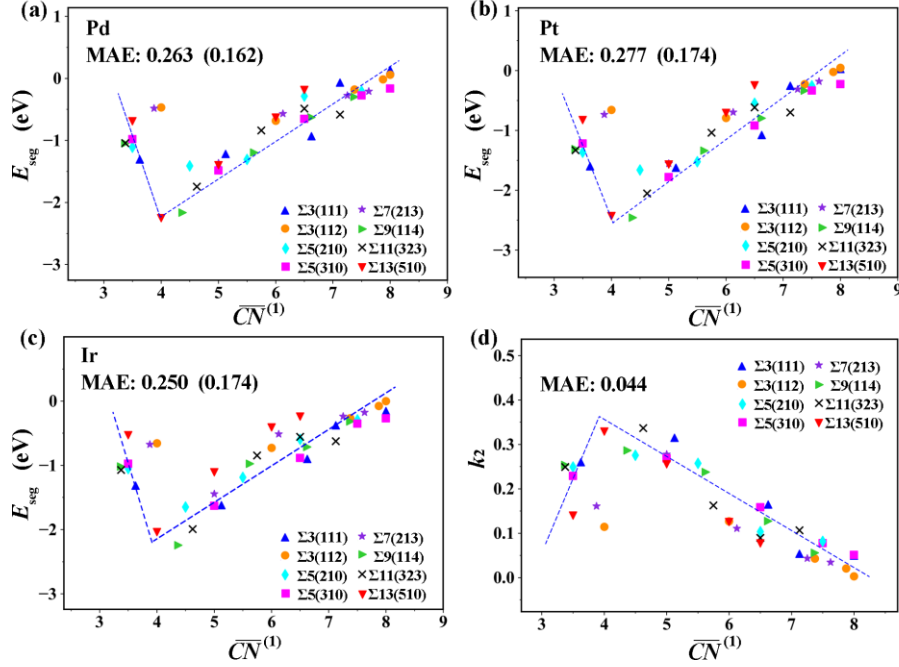


Fig. 4 The segregation energies and the slope k_2 as a function of $\overline{CN}^{(1)}$. (a) Pd solute, (b) Pt solute and (c) Ir solute. The MAE in parentheses is the accuracy without the two outliers. (d) The slope k_2 of the D_{seg} determined scaling relation against $\overline{CN}^{(1)}$ for all the involved segregation sites.

$E_{\text{seg}} = -k_2(2D_{\text{seg}} + 1)$ for the group 1 solutes and $E_{\text{seg}} = -k_2\left(\frac{D_{\text{seg}}}{3} + 2\right)$ for the group 3 solutes. Our scheme uncovers a unique and simple physical picture for the coupling between solutes and matrices, that is, via the electronic bonding and size effect of solutes and the geometric effect of GBs. Moreover, the involved parameters S_v , χ , R and $\overline{CN}^{(1)}$ are easily accessible by table looking up and thus convenient for the practical application. The MAE of this model is 0.10 eV for all the involved 8 GBs of W matrix (each with 5 segregation sites) and 29 TM solutes. In addition, the MAE is about 0.10 eV for 11 Al GBs ($\Sigma 3(111)$, $\Sigma 3(112)$, $\Sigma 5(310)$, $\Sigma 9(221)$, $\Sigma 11(113)$, $\Sigma 13(320)$, $\Sigma 17(410)$, $\Sigma 17(223)$, $\Sigma 19(331)$, $\Sigma 27(115)$ and $\Sigma 43(335)$ GB), 0.14 eV for Ni GBs ($\Sigma 5(210)$), 0.16 eV for 2 Mo GBs ($\Sigma 5(100)$ twist and $\Sigma 5(310)$ tilt) and 0.12 eV for Zr GBs ($\Sigma 13(10\bar{1}1)$). These results demonstrate that our scheme is universal and predictive in determining the segregation energies across different TM solutes, matrices, GB structures and segregation sites.

Our scheme can also deduce or rationalize the experimental segregation tendency. The experimental results in W show that there is almost no segregation for Ti or Ta solutes at GBs, whereas Ag solute is prone to segregate to all sites around GBs.³⁸ These observations likely stem from the fact that the Ti/Ta and Ag solutes sit close to the turning points of our scheme, the top and bottom respectively. More importantly, combining our scheme with the White-Coghlan model³⁹, one can also predict the GB concentration (c_{GB}) curves for non-interacting solutes, which is determined as:

$$c_{\text{GB}} = \frac{1}{N} \sum_{i=1}^N \frac{1}{1 + \frac{1 - c_{\text{bulk}}}{c_{\text{bulk}}} \exp\left(-\frac{E_{\text{seg}}^{X,i}}{k_{\text{B}}T}\right)} \quad (4)$$

where N represents the total number of segregation sites (fixed as 5 here), $E_{\text{seg}}^{X,i}$ is the segregation energy of solute X segregated to the position i at GBs and T is temperature. c_{bulk} is the concentration in the matrix, which is fixed as 2 at.% here^{18,20}. Fig. 5 and Supplementary Fig. 10 show that the predicted GB concentrated curves based on our framework are close to the DFT-calculated ones across a wide temperature range regardless of solutes and GB structures, further verifying the validity of our framework. Compared with the late TM solutes, the early TM solutes have the solute concentrate depending more strongly on temperature, suggesting temperature as an effective way to engineer the early TM solutes at GBs.

Discussion

Overall, our framework provides an effective tool to analyze the solute segregation behavior for various solutes and GB structures with the accessible intrinsic properties. The proposed descriptor D_{seg} exhibits wide applicability across TM and main-group solutes in the various matrices even polycrystals, essentially implying the local effects of solute atoms and the similar matrix deformation with different solute atoms. Even with the significant different deformation and relaxation for different solute atoms in single-crystal matrices, the coupling item $D_{\text{seg}}\overline{CN}^{(1)}$ most

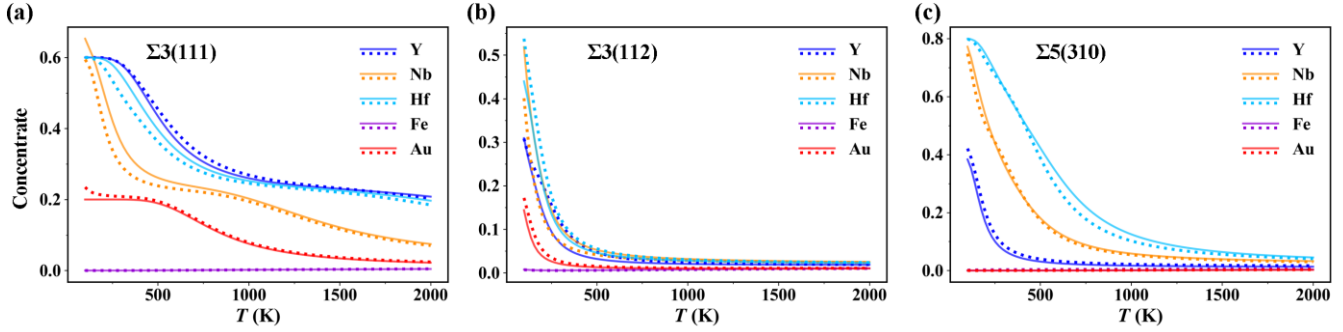


Fig. 5 The predicted and DFT-calculated GB concentrate curves based on the White-Coghlan model. (a) $\Sigma 3(111)$ GB, (b) $\Sigma 3(112)$ GB and (c) $\Sigma 5(310)$ GB. The solid curves are obtained with the segregation energies predicted from our model and the dotted lines are obtained with the DFT-calculated segregation energies.

likely holds for describing the segregation energies. In contrast, $\overline{CN}^{(1)}$ reflects the non-local effects of segregation sites at GBs and is well suited to single-crystal matrices. For polycrystal matrices, one may introduce more complicated geometric features such as bond length and angle to characterize the geometric structures of GBs, which will thus be a natural extension of this study.

In summary, we have identified the four main factors that control the segregation energies of solutes at GBs: the valence, electronegativity and size of solutes and the non-local coordination number of free matrix surfaces. This enables us to build a predictive framework to quantitatively determine the segregation energies, which holds across the different solutes, matrices, GBs and segregation sites. The determinant of solutes, initially inspired by the tight-binding model, reflects the coupling of d- and s-states of solutes in alloying, whereas that of GB matrices, indicating a non-local geometric effect, does the free-surface-determined nature of GB interfaces. Our framework uncovers the electronic origin for the behavior of alloying elements in GB segregation, the connection between free surfaces and their resulting GB interfaces, and the coupling mechanism of solutes and GB matrix, all of which propose a simple and clear physical picture for the solute segregation at GBs. All these findings are thus expected to serve as quantitative guidelines for the future alloy design, particularly considering that all involved parameters are predictable.

Method

Our calculations are performed using Vienna ab-initio simulation package (VASP) code⁴⁰. The interaction between ions and electrons is described by the projector augmented wave potential (PAW) method⁴¹. The exchange and correlation functions are taken for the generalized gradient approximation (GGA)⁴². The cutoff energy of 500 eV is used in the calculations and the k-point mesh is given in Supplementary Table 4. The cell volume and atomic position are relaxed for each GB supercell without solutes and then kept fixed when the solutes are inserted. For the optimization, all the atoms are relaxed until the forces on each of them are less than 0.02 eV/atom in our calculations.

The symmetric tilt grain boundaries are constructed by using the coincidence site lattice (CSL) model⁴³. We construct 8 low- Σ symmetric tilt W GBs with [001], [110] and [111] tilt axes. The slabs are separated with 10 Å of vacuum to exclude interactions between periodic images. The grains that are used to construct the W GBs contain the six layers for $\Sigma 3(111)$, $\Sigma 3(112)$, $\Sigma 5(210)$ and $\Sigma 5(310)$ GBs, and nine layers for $\Sigma 7(213)$, $\Sigma 9(114)$, $\Sigma 11(323)$ and $\Sigma 13(510)$ GBs. The data of tilt angles, layers and atom numbers are also listed in Supplementary Table 4. We also study the 8 tilt W GBs with structural optimization during solute segregation, the data of which are from Ref. [5]. Moreover, we study the segregation energies in the GB structures of Zr³³, Ni^{34,35}, Mo¹⁷ and Al³². The GBs of the polycrystal Ag, Au, Cu, Fe, Co, Ni, Mo, W, Pd, Pt, Ti, Zr, Ta, Mg and Al matrices are also considered for segregation¹⁹.

The segregation energy E_{seg} is defined as:

$$E_{\text{seg}} = E_{\text{GB}} - E_{\text{Bulk}} \quad (5)$$

where E_{GB} is the total energy of the structure with the solute atoms at GBs and E_{Bulk} is the total energy of the structure with the solute atom inside the bulk.

References

1. King, A., Johnson, G., Engelberg, D., Ludwig, W. & Marrow, J. Observations of intergranular stress corrosion cracking in a grain-mapped polycrystal. *Science* **321**, 382-385 (2008).
2. Mishin, Y., Asta, M. & Li, J. Atomistic modeling of interfaces and their impact on microstructure and properties. *Acta Mater.* **58**, 1117-1151 (2010).
3. Nie, J. F., Zhu, Y. M., Liu, J. Z. & Fang, X. Y. Periodic segregation of solute atoms in fully coherent twin boundaries. *Science* **340**, 957-960 (2013).
4. Herbig, M., Raabe, D., Li, Y. J., Choi, P., Zaefferer, S. & Goto, S. Atomic-scale quantification of grain boundary segregation in nanocrystalline material. *Phys. Rev. Lett.* **112**, 126103 (2014).
5. Wu, X. B., You, Y. W., Kong, X. S., Chen, J. L., Luo, G. N., Lu, G. H., Liu, C. S. & Wang, Z. G. First-principles determination of grain boundary strengthening in tungsten: Dependence on grain boundary structure and

- metallic radius of solute. *Acta Mater.* **120**, 315-326 (2016).
6. Huang, Z. F., Wang, P., Chen, F., Shen, Q. & Zhang, L. M. Understanding solute effect on grain boundary strength based on atomic size and electronic interaction. *Sci. Rep.* **10**, 16856 (2020).
 7. Jin, H., Elfimov, I. & Militzer, M. Study of the interaction of solutes with $\Sigma 5$ (013) tilt grain boundaries in iron using density-functional theory. *J. Appl. Phys.* **115**, 093506 (2014).
 8. Čák, M., Šob, M. & Hafner, J. First-principles study of magnetism at grain boundaries in iron and nickel. *Phys. Rev. B* **78**, 054418 (2008).
 9. Kong, X. S., Wu, X. B., You, Y. W., Liu, C. S., Fang, Q. F., Chen, J. L., Luo, G. N. & Wang, Z. G. First-principles calculations of transition metal-solute interactions with point defects in tungsten. *Acta Mater.* **66**, 172-183 (2014).
 10. Huber, L., Grabowski, B., Militzer, M., Neugebauer, J. & Rottler, J. Ab initio modelling of solute segregation energies to a general grain boundary. *Acta Mater.* **132**, 138-148 (2017).
 11. Scheiber, D., Romaner, L., Pippan, R. & Puschnig, P. Impact of solute-solute interactions on grain boundary segregation and cohesion in molybdenum. *Phys. Rev. Mater.* **2**, 093609 (2018).
 12. Wagih, M. & Schuh, C. A. Spectrum of grain boundary segregation energies in a polycrystal. *Acta Mater.* **181**, 228-237 (2019).
 13. McLean, D. Grain boundaries in metals. *Oxford University Press* (1957).
 14. Miedema, A. R. Surface segregation in alloys of transition-metals. *Int. J. Mater. Res.* **69**, 455-4611 (1978).
 15. Murdoch, H. A. & Schuh, C. A. Estimation of grain boundary segregation enthalpy and its role in stable nanocrystalline alloy design. *J. Mater. Res.* **28**, 2154-2163 (2013).
 16. Scheiber, D., Pippan, R., Puschnig, P., Ruban, A. & Romaner, L. Ab-initio search for cohesion-enhancing solute elements at grain boundaries in molybdenum and tungsten. *Int. J. Refract. Met. Hard Mater.* **60**, 75-81 (2016).
 17. Tran, R., Xu, Z. H., Zhou, N. X., Radhakrishnan, B., Luo, J. & Ong, S. P. Computational study of metallic dopant segregation and embrittlement at molybdenum grain boundaries. *Acta Mater.* **117**, 91-99 (2016).
 18. Huber, L., Hadian, R., Grabowski, B. & Neugebauer, J. A machine learning approach to model solute grain boundary segregation. *Npj Comput. Mater.* **4**, 64 (2018).
 19. Wagih, M., Larsen, P. M. & Schuh, C. A. Learning grain boundary segregation energy spectra in polycrystals. *Nat. Commun.* **11**, 6376 (2020).
 20. Hu, Y. J., Zhao, G., Zhang, B. Y., Yang, C. M., Zhang, M. F., Liu, Z. K., Qian, X. F. & Qi, L. Local electronic descriptors for solute-defect interactions in bcc refractory metals. *Nat. Commun.* **10**, 4484 (2019).
 21. Ruban, A. V., Skriver, H. L. & Norskov, J. K. Surface segregation energies in transition-metal alloys. *Phys. Rev. B* **59**, 15990-16000 (1999).
 22. Xu, Z., Tanaka, S. & Kohyama, M. Grain-boundary segregation of 3d-transition metal solutes in bcc Fe: Ab initio local-energy and d-electron behavior analysis. *J. Phys.-Condens. Mat.* **31**, 115001 (2019).
 23. Huber, L., Rottler, J. & Militzer, M. Atomistic simulations of the interaction of alloying elements with grain boundaries in mg. *Acta Mater.* **80**, 194-204 (2014).
 24. Pettifor, D. G. On the tight binding theory of the heats of formation. *Solid State Commun.* **28**, 621-623 (1978).
 25. Friedel, J. The physics of metals. *Cambridge University Press, New York*, 512 (1969).
 26. Turchanin, M. A. & Agraval, P. G. Cohesive energy, properties, and formation energy of transition metal alloys. *Powder Metall. Met. Ceram.* **47**, 26-39 (2008).
 27. Gao, W., Chen, Y., Li, B., Liu, S. P., Liu, X. & Jiang, Q. Determining the adsorption energies of small molecules with the intrinsic properties of adsorbates and substrates. *Nat. Commun.* **11**, 1196 (2020).
 28. Li, B., Li, X., Gao, W. & Jiang, Q. An effective scheme to determine surface energy and its relation with adsorption energy. *Acta Mater.* **212**, 116895 (2021).
 29. Verlet, V. Computer "experiments" on classical fluids. I. Thermodynamical properties of Lennard-Jones molecules. *Phys. Rev.* **159**, 98-103 (1967).
 30. Wachowicz, E., Ossowski, T. & Kiejna, A. Cohesive and magnetic properties of grain boundaries in bcc Fe with Cr additions. *Phys. Rev. B* **81**, 094104 (2010).
 31. Tschopp, M. A., Solanki, K. N., Gao, F., Sun, X., Khaleel, M. A. & Horstemeyer, M. F. Probing grain boundary sink strength at the nanoscale: Energetics and length scales of vacancy and interstitial absorption by grain boundaries in α -Fe. *Phys. Rev. B* **85**, 064108 (2012).
 32. Mahjoub, R., Laws, K. J., Stanford, N. & Ferry, M. General trends between solute segregation tendency and grain boundary character in aluminum - an ab initio study. *Acta Mater.* **158**, 257-268 (2018).
 33. Xue, Z., Zhang, X. Y., Qin, J. Q., Ma, M. Z. & Liu, R. P. Exploring the effects of solute segregation on the strength of Zr $\{10\bar{1}1\}$ grain boundary: A first-principles study. *J. Alloys Compd.* **812**, 152153 (2020).
 34. Razumovskiy, V. I., Lozovoi, A. Y. & Razumovskii, I. M. First-principles-aided design of a new Ni-base superalloy: Influence of transition metal alloying elements on grain boundary and bulk cohesion. *Acta Mater.* **82**, 369-377 (2015).
 35. Razumovskiy, V. I., Lozovoi, A. Y. & Razumovskii, I. M. First-principles-aided design of a new Ni-base superalloy: Influence of transition metal alloying elements on grain boundary and bulk cohesion (*Acta Mater.* **82**, 369-377 (2015)). *Acta Mater.* **106**, 401-402 (2016).

36. Calle-Vallejo, F., Martinez, J. I., Garcia-Lastra, J. M., Sautet, P. & Loffreda, D. Fast prediction of adsorption properties for platinum nanocatalysts with generalized coordination numbers. *Angew. Chem. Int. Ed.* **53**, 8316-8319 (2014).
37. Calle-Vallejo, F., Tymoczko, J., Colic, V., Vu, Q. H., Pohl, M. D., Morgenstern, K., Loffreda, D., Sautet, P., Schuhmann, W. & Bandarenka, A. S. Finding optimal surface sites on heterogeneous catalysts by counting nearest neighbors. *Science* **350**, 185-189 (2015).
38. AlMotasem, A. T., Huminiuc, T. & Polcar, T. Factors controlling segregation tendency of solute Ti, Ag and Ta into different symmetrical tilt grain boundaries of tungsten: First-principles and experimental study. *Acta Mater.* **211**, 116868 (2021).
39. White, C. L. & Coghlan, W. The spectrum of binding energies approach to grain boundary segregation. *Metall. Trans. A* **8**, 1403-1412 (1977).
40. Kresse, G. & Furthmüller, J. Efficient iterative schemes for ab initio total-energy calculations using a plane-wave basis set. *Phys. Rev. B* **54**, 11169-117979 (1996).
41. Blöchl, P. E. Projector augmented-wave method. *Phys. Rev. B* **50**, 17953-17979 (1994).
42. Perdew, J. P., Burke, K. & Ernzerhof, M. Generalized gradient approximation made simple. *Phys. Rev. Lett.* **77**, 3865-3868 (1996).
43. Grimmer, H. Coincidence-site lattices. *Acta Crystallogr. Sect. A* **32**, 783-785 (1976).

Acknowledgments

The authors are thankful for the support from the National Natural Science Foundation of China (Nos. 22173034, 11974128, 52130101), the Opening Project of State Key Laboratory of High Performance Ceramics and Superfine Microstructure (SKL201910SIC), the Program of Innovative Research Team (in Science and Technology) in University of Jilin Province, the Program for JLU (Jilin University) Science and Technology Innovative Research Team (No. 2017TD-09), the Fundamental Research Funds for the Central Universities, and the computing resources of the High Performance Computing Center of Jilin University, China.

Author information

*Email: wgao@jlu.edu.cn

Author contributions

W.G. and Q.J. conceived the original idea and designed the strategy. X.L. performed the DFT calculations. W.G. derived the models and analyzed the results with the contribution from X.L. X.L. and W.G. wrote the manuscript. X.L. prepared the Supplementary Information and drew all figures. All authors have discussed and approved the results and conclusions of this article.

Competing interests

The authors declare no competing interests.